

PAPER • OPEN ACCESS

Experimental investigation into efficiency loss in rotating magnetic field thrusters

To cite this article: T M Gill *et al* 2024 *Plasma Sources Sci. Technol.* **33** 015006

View the [article online](#) for updates and enhancements.

You may also like

- [Miniaturized rotating magnetic field-driven plasma system: proof-of-concept experiments](#)

Y Sun, I Levchenko, J W M Lim *et al.*

- [Electron- versus neutrino-nucleus scattering](#)

J E Amaro, M B Barbaro, J A Caballero *et al.*

- [Development of featured high-density helicon sources and their application to electrodeless plasma thruster](#)

Shunjiro Shinohara, Daisuke Kuwahara, Takeru Furukawa *et al.*

HIDEN
ANALYTICAL

Analysis Solutions for your **Plasma Research**

- Knowledge
- Experience ■ Expertise

[Click to view our product catalogue](#)

Contact Hiden Analytical for further details:

www.HidenAnalytical.com
info@hiden.co.uk



Surface Science

- ▶ Surface Analysis
- ▶ SIMS



- ▶ 3D depth Profiling
- ▶ Nanometre depth resolution



Plasma Diagnostics

- ▶ Plasma characterisation
- ▶ Customised systems to suit plasma Configuration



- ▶ Mass and energy analysis of plasma ions
- ▶ Characterisation of neutrals and radicals

Experimental investigation into efficiency loss in rotating magnetic field thrusters

T M Gill* , C L Sercel  and B A Jorns 

Department of Aerospace Engineering, University of Michigan, 1320 Beal Avenue, Ann Arbor, MI 48109-2140, United States of America

E-mail: tategill@umich.edu

Received 19 May 2023, revised 16 November 2023

Accepted for publication 28 November 2023

Published 17 January 2024



CrossMark

Abstract

An experimental investigation into the low thrust efficiency of a rotating magnetic field (RMF) thruster is presented. This technology is a low maturity but potentially enabling candidate for high-power in-space propulsion for use with alternative propellants. Direct thrust stand measurements of a 5 kW class RMF thruster were performed and show the thrust efficiency was $0.41 \pm 0.04\%$ with a specific impulse of 292 ± 11 s—typical values for RMF thruster operation. A suite of far-field probes were used to inform a phenomenological efficiency model for RMF thruster performance that accounted for divergence, power coupling, mass utilization, and plasma/acceleration efficiency. It was found that the plasma efficiency was the critically low term at $6.4 \pm 1.0\%$. This indicates that the majority of the energy coupled to the plasma from the RMF antennas was lost before being converted to directed kinetic energy in the thruster beam. To determine the source of these losses, time-resolved measurements of the internal plasma properties were performed using a triple Langmuir probe. It was found that collisional excitation radiation and wall losses were the two dominant loss processes. This trend can be explained by the unusually high plasma density ($>10^{19} \text{ m}^{-3}$) exhibited by this device compared to other electric propulsion architectures. Limitations in the probing techniques and strategies for improving RMF thruster performance are discussed given the results from the efficiency analysis.

Keywords: electric propulsion, inductive pulsed plasma thrusters, rotating magnetic field thrusters, magnetic nozzles

1. Introduction

Inductive pulsed plasma thrusters (IPPTs) are an attractive technology for next-generation electric propulsion

applications. In short, these devices utilize fast current transients to induce mirror currents in a plasma which drive Lorentz force acceleration [1]. A key advantage of this approach, in contrast to more conventional thruster technologies like Hall and gridded thrusters, is that it does not necessitate the use of plasma-wetted electrodes. This class of EP technology thus has the ability to operate on alternative—and more chemically reactive—propellants such as those recovered from in-situ resource utilization or through sharing fuel with chemical propulsion systems in dual mode architectures [2]. IPPTs also exhibit favorable high power scaling because the impulse

* Author to whom any correspondence should be addressed.



Original Content from this work may be used under the terms of the [Creative Commons Attribution 4.0 licence](https://creativecommons.org/licenses/by/4.0/). Any further distribution of this work must maintain attribution to the author(s) and the title of the work, journal citation and DOI.

they produce trends quadratically with the driven plasma current due to their magnetic acceleration mechanism [1]. Furthermore, because these thrusters operate in a pulsed mode, they can be throttled across a wide power range by varying the pulse repetition frequency.

These attributes make IPPTs a promising high-power option for electric propulsion, and historically, laboratory model IPPTs have demonstrated competitive performance metrics to those of state-of-the-art EP thrusters. For instance, the pulsed inductive thruster (PIT) achieved up to 7000 s specific impulse at 50% thrust efficiency [3, 4]. Despite these promising results, however, IPPTs face several key challenges for their adoption for flight. Most critically, to achieve the quoted efficiencies, PIT required the use of very large transient voltages—between 30 and 60 kV pulsed over microseconds—as well as sensitive pulsed gas injection valves and pre-ionization schemes.

The rotating magnetic field (RMF) thruster has however the potential to overcome the limitations of archetypical IPPTs through an alternate plasma current drive method. RMF thrusters do not rely on large transient pulses to induce currents in the plasma. Instead, they leverage high frequency phasing of multiple coils to achieve the time-varying magnetic fields needed for inductive current drive. As a result, they can drive high levels of electron current (>kA) at reduced voltages.

In light of this advantage over other inductive thruster architectures, there have been several previous efforts to investigate RMF devices. Mathematical Sciences Northwest (MSNW) developed multiple test articles demonstrating pulse energies up to 50 J on gases including nitrogen and xenon [5–8]. Tokyo University of Agriculture and Technology implemented another RMF device intended to run semi-continuously at 1 kW on argon [9, 10]. At the University of Michigan, we recently built and characterized a test article that demonstrated steady-state operation at 150 pulses per second and powers up to 4.5 kW operating on xenon. While these systems differed in implementation and scale, in all cases, RMF performance was poor with efficiencies of $\sim 1\%$. The highest reported efficiency to date was 8% from MSNW, but we note this value may be an overestimate given it did not include typical divergence or antenna coupling losses. These results underscore the nascence of the technology, given that the maximum RMF thruster efficiency is predicted to be as high 85% [5].

The systematic poor performance of RMF technology invites the question as to what processes are inhibiting efficient operation. It has been suggested, for example, that radiative losses [6] or poor mass utilization [11] may explain this behavior. With that said, there is a lack of direct experimental data to assess what drives the efficiency loss. Moreover, for the data that has been previously generated, either the diagnostics had limited accessibility [9, 10] or the test articles in question were operated in facilities that were not representative of the on-orbit environment where these devices are intended to operate [5–8]. Given the outstanding fundamental questions about the operation of RMF thrusters, there is an apparent need for a detailed experimental characterization of the efficiency modes of the performance of an RMF device operating under more space-like conditions.

The goal of this work is to leverage conventional phenomenological models of other electric propulsion devices [12–14] combined with both near and far-field plasma diagnostics to directly measure the contributions of various efficiency losses in a 5 kW class RMF thruster. To this end, this paper is organized in the following way. We begin by deriving a phenomenological efficiency breakdown for RMF thrusters. Next, we describe the experimental setup, the test article, and the diagnostic measurements. Finally, we discuss the results of our measurements and interpret them as they pertain to overall thruster efficiency and performance.

2. Theory of RMF thruster operation

In this section we overview the operation of an RMF thruster including further details on the advantages of this architecture over other IPPTs. Following this, we describe the phenomenological efficiency breakdown we employ in the remainder of this work.

2.1. Principle of operation

We show in figure 1 the canonical geometry and principle of operation for an RMF thruster. In this device, gas flows into the thruster volume, and a fraction of this inlet flow is ionized into a seed plasma by a cathode or pre-ionizer. The resulting ionized particles are confined by a primarily longitudinal magnetic field provided by a series of concentric bias magnets. Two sets of orthogonal Helmholtz configuration antennas—the RMF antennas—are then pulsed in a controlled sequence to produce a near-uniform transverse magnetic field that rotates about the primary axis of the thruster—the RMF. The RMF is produced at a sufficiently high frequency to selectively entrain the electrons in the seed plasma. These field-lined electrons travel at the RMF frequency further ionizing the neutral propellant, and form an azimuthal plasma current relative to the background ions. For sufficiently strong amplitudes of the RMF relative to the plasma density, this azimuthal current is independent of the magnitude of the RMF antenna current [15]:

$$I_{\theta} = \frac{eN_e\omega}{2\pi}, \quad (1)$$

where N_e is the number of electrons, and ω is the RMF frequency. As this scaling shows, in principle, the current driven in RMF thrusters is only a function of the total number of free electrons and the frequency of the RMF. This is in contrast to conventional IPPTs where the induced current relies on the rapid discharge of high amplitude voltages [3, 4, 16]. The reduction in required voltages for the RMF significantly reduces the stress on the driving circuitry, which better favors scaling to high powers and duty cycles.

The ring of induced azimuthal electron current accelerates from the thruster via the Lorentz force. This force results from interactions with radial components of both the applied bias field as well as the time-varying magnetic fields in the surrounding structure (which are in turn induced by the azimuthal

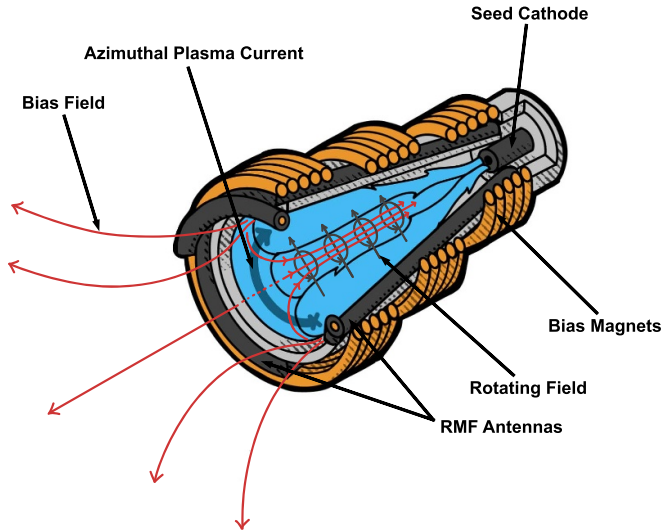


Figure 1. Operational principles of the rotating magnetic field thruster.

electron current) [17]. The electrons drag the heavier ions out of the geometry through ambipolar electric fields. This process results in an impulse ‘per shot’:

$$J \propto \int I_{\theta} \langle B_r \rangle dt, \quad (2)$$

where $\langle B_r \rangle$ is a spatially averaged magnetic field arising from both the applied field and self-field effects. The generation of impulse shots can be repeated continuously in a pulsed manner to deliver quasi-steady-state thrust. In principle, the time scale of acceleration of a single pulse is a small fraction of the overall pulse rate. As a result, the physics of a single pulse remains independent of pulse rate. This is another major advantage of pulsed devices, where efficiency and specific impulse can be maintained while thrust is throttled by changing the frequency of pulsing.

2.2. Efficiency model

In this section, we represent the total efficiency of the RMF thruster as a product of key energy loss modes. We formulate our model in terms of the efficiency of impulse imparted per shot of the thruster. This therefore is an indication of the ability to convert total energy delivered in a pulse to the total jet energy:

$$\eta = \frac{J^2}{2ME_{in}}, \quad (3)$$

where M is the cumulative propellant mass and E_{in} is the input electrical energy per shot. We note this is equivalent to the conventional jet power efficiency of a steady-state thruster.

We in turn can represent the impulse efficiency in terms of constituent elements:

$$\eta = \eta_d \eta_m \eta_c \eta_p, \quad (4)$$

where, η_d is the divergence efficiency, η_m is the mass utilization efficiency, η_c is the coupling efficiency, and η_p is the plasma efficiency.

The divergence efficiency in this expression, η_d , is a measure of the reduction in thrust generation caused by the existence of radial ion velocity in the accelerated plasmoid:

$$\eta_d = \left(\frac{J}{J_{beam}} \right)^2 = \cos^2 \Theta. \quad (5)$$

Here, J is the imparted axial impulse, and J_{beam} is the total momentum flux in the ion beam spherically leaving the thruster. We also have noted here that divergence efficiency can be expressed in terms of a characteristic divergence angle, Θ , which is measured with respect to the symmetry axis of the thruster. For larger divergence angles, i.e. scenarios in which more momentum is directed radially outward, the divergence efficiency suffers.

The mass utilization efficiency, η_m , represents how effectively the thruster can ionize and accelerate the neutral propellant:

$$\eta_m = \frac{M_i}{M}, \quad (6)$$

where M_i is the total ejected ion mass for a single pulse. For lower effective ionization fractions, this efficiency decreases.

The coupling efficiency, η_c , is related to the energy consumed by the resistance of the RMF antennas and power processing system:

$$\eta_c = \frac{E_p}{E_{in}}, \quad (7)$$

where E_p is the energy absorbed by the plasma. This efficiency is a measure of how effectively the RMF system supplies energy to the plasma. For larger circuit resistances or poorer energy coupling to the plasma, this efficiency decreases.

In practice, the total energy absorbed by the action of the RMF on the plasma can contribute to multiple modes. This can stem from direct acceleration of the plasma through an axial Lorentz force, from compression of the plasma by a radial Lorentz force, or from heating of the electrons arising from viscous drag of the RMF current against the heavier species. This latter heating in turn can be lost to the walls or can contribute to frozen flow losses like ionization and radiation. To represent all these effects, we express the energy in the plasma as

$$E_p = \frac{J_{beam}^2}{2M_i} + E_{th} + E_{iz} + E_{wall} + E_{rad}, \quad (8)$$

where $J_{beam}^2/2M_i$ is the momentum-carrying energy from the forces acting on the plasma, E_{th} is the thermal energy of the ions in the ion beam, E_{iz} is ionization energy cost, E_{wall} is the energy lost due to electrons recombining at the wall, and E_{rad} is the optical power emitted from inelastic electron collisions with heavy species.

With this definition of total plasma energy in mind, we define finally the plasma efficiency, η_p , as the proportion of

the energy coupled into the plasma that is converted into directed kinetic energy:

$$\eta_p = \frac{J_{\text{beam}}^2}{2M_i E_p}. \quad (9)$$

Physically, this mode reflects the relative fraction of useful energy for thrust generation compared to the total energy.

In summary, the four phenomenological efficiency modes outlined in equation (4) provide a framework to examine RMF thruster performance. The goal for this work is to measure each one experimentally with plasma diagnostic techniques.

3. Experimental setup

In this section, we summarize the experimental setup including details on the RMF thruster and power processing unit (PPU) as well as descriptions of the diagnostics we used to characterize the efficiency modes from section 2.2.

3.1. Test Article and power processing unit

Figure 2(a) shows an image of the test article we employed for this investigation—the 5 kW class PEPL RMFv2. During operation, xenon gas is injected into a conical volume bounded by a mica surface through the aperture of an upstream hollow cathode as well as from an upstream-facing annular neutral injector at the thruster exit plane. The conical thruster body is characterized by a cone with a half angle of 14° , a 20 cm exit diameter, and a length of 33 cm. A 60 A-class LaB₆ hollow cathode provides a seed plasma which is confined by the magnetic field generated by an array of three DC air-core solenoid electromagnets concentric to the cone (see figure 2(a)). These are capable of generating magnetic fields up to 240 G on thruster centerline. Two orthogonal Helmholtz pair antennas extend along the geometry external to the cone. These are pulsed 90° out of phase to generate the RMF. The majority of the thruster structure is constructed from dielectric FR4 and G10 fiberglass to minimize coupling losses to the structure [18]. Additional details on the design of the test articles can be found in [19].

The RMF is generated by a PPU developed by Eagle Harbor Technologies [20]. This PPU employs a resonant sine inverter, where each of the two RMF antennas is connected in series to a 40 nF resonant capacitor bank located next to the thruster. This forms an LC circuit which we drive at its resonant frequency with a full bridge solid state switching unit to produce kiloamp-level currents through the antennas.

We perform the measurements in this investigation with the thruster at a fixed operating condition that we have found from previous exploratory work yielded the maximum in thruster efficiency. This condition consisted of a 4.0 mg s^{-1} xenon total flow rate with a 33% cathode flow fraction, 18 A cathode discharge current, 180 G peak DC magnetic field, 2.0 kA pk-pk RMF currents, 125 μs pulse duration, RMF frequency of 415 kHz, and pulse repetition rate of 155 Hz.

We show in figure 2(b) a long exposure image of the thruster firing at a similar operating condition to the one we

examined in this work. The luminance from the thruster diffusely extends downstream (roughly 10 cm) with a large radial expansion from the upstream cone. As this image is time-averaged over ~ 1500 pulses, it does not capture the transient behavior of the plasmoid. However, previous high speed imaging has shown that the plasma forms a ‘D-shaped’ structure that is expelled from the thruster [19]. The time-integrated light intensity approximately reflects this shape.

3.2. Diagnostics

For this study, we employed a suite of diagnostic tools to evaluate thruster performance and plasma properties. To measure the quasi-steady thrust, we used a displacement mode inverted pendulum thrust stand calibrated to yield values ranging from 0–20 mN with a relative uncertainty of 0.5 mN (see section 4.2). Additionally, we measured the current waveforms through the RMF antennas using 0.1 V A^{-1} wide-band Pearson coils paired with 10:1 compensated oscilloscope probes.

The far-field ion current density was measured using a guarded Faraday probe (FP). This consisted of a 1.74 cm molybdenum collector and an annular 0.54 cm molybdenum guard ring with a 0.05 cm gap between them. Both the collector and guard were biased to -115 V relative to facility ground to ensure that ion saturation was achieved. The need for such large negative potentials to repel electrons is documented in other RF thrusters [21] and is indirect evidence of some population of high energy electrons. The use of a guarded FP flattens the ion sheath to mitigate the effect of sheath expansion on our measurements. To measure the time-varying electron density and temperature inside the thruster, we utilized a triple Langmuir probe (TLP) [22]. Our TLP was made from three 0.127 mm diameter by 1.270 mm long thoriated tungsten rods with 2 mm spacing between them. One of these electrodes was electrically floating and the other two electrodes were biased to 28.8 V with respect to each other. Current was measured between the biased probes with a wide-band Pearson coil, and voltage was measured between the floating and positively biased electrodes with a 50:1 floating differential probe. We evaluated the azimuthal currents produced in the plasma from the RMF with spatially resolved measurements made with a two-axis B-dot probe. The details of this computation are presented in another paper [23].

Signals from all plasma diagnostic probes were sampled at 1 MHz using a 16 bit digital oscilloscope and were passed through 4th order RC low-pass filters to attenuate noise from the RMF. The corner frequency of these filters was 100 kHz and is thus the effective bandwidth of our measurements. During operation, we utilized the periodic nature of the RMF pulses to synchronize measurements across shots. This enabled us to reduce noise through averaging and to time-align probe measurements at different locations in the plasma. In general, the uncertainty of our probe measurements was driven by the shot-to-shot variance of the pulses. Special cases where additional uncertainty was taken into account are discussed further in section 5.

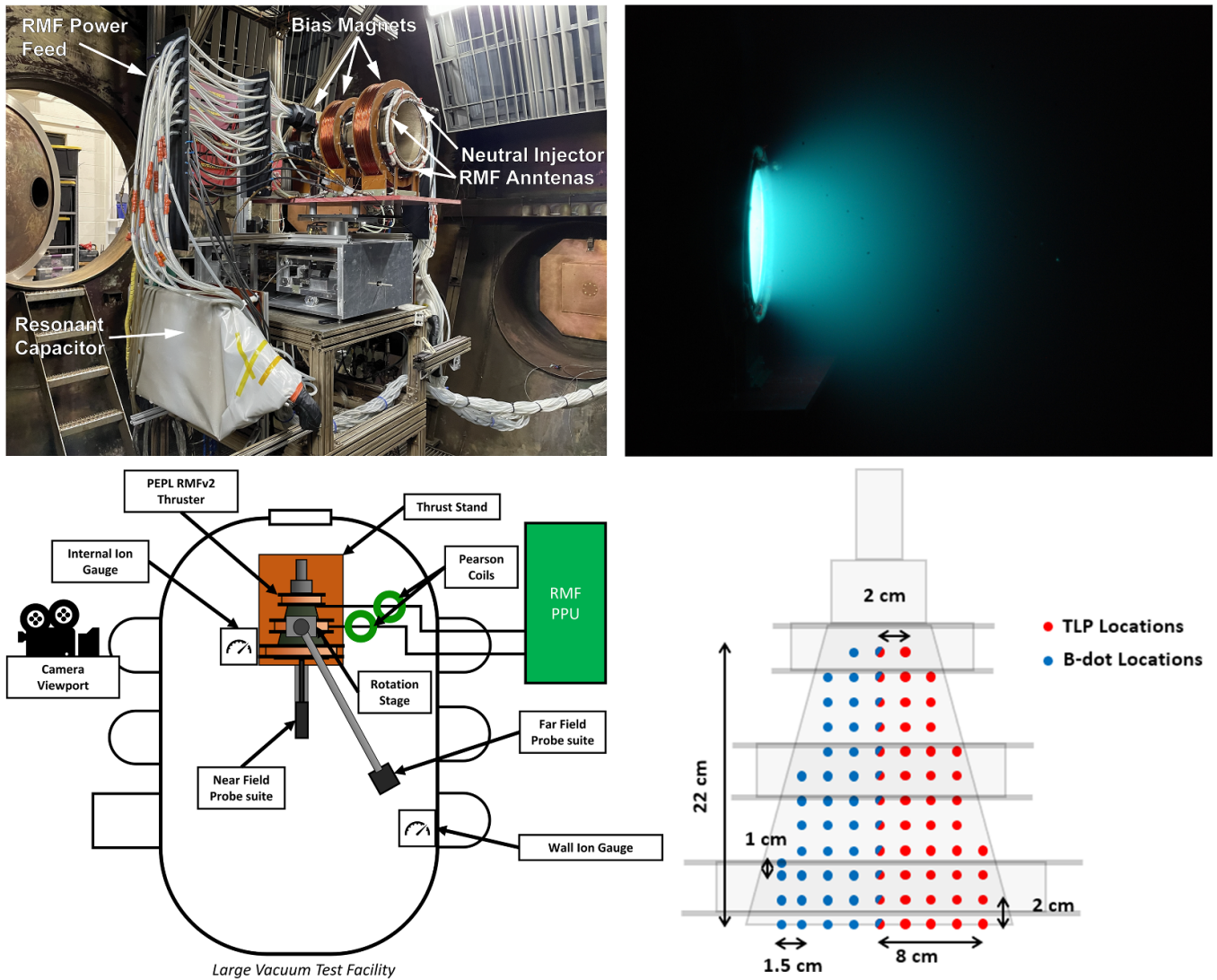


Figure 2. (a) Experimental setup of thruster in vacuum facility. (b) Long exposure image (10 s) of thruster firing, note: alternate operating condition with $200 \mu\text{s}$ pulse length and 120 G magnetic field strength. (c) Schematic of experimental setup with notional locations of diagnostics. (d) Internal measurement locations of TLP and B-dot probes.

3.3. Test facility and measurement locations

We show in figure 2(c) a schematic of the thruster and diagnostics inside the vacuum test facility. The experiments described here were performed at the large vacuum test facility at the University of Michigan. During testing, the background pressure was on the order of 2×10^{-6} Torr Xe and was monitored using a Stabil ion gauge located 1 m radially from the thruster in the thruster’s exit plane in accordance with best practices for electric propulsion testing [24]. The far-field FP measurements were performed in a polar arc about the center of the thruster exit plane. This arc had a radius of 1.72 m and data was collected at 5° increments from -90° to 90° , where zero degrees corresponded to the thruster axis. We employed a two-axis motion stage in the thruster near-field to take measurements with the B-dot probes and TLP. Each probe was translated on a horizontal plane coincident with the thruster axis inside the thruster volume with measurements made on an

approximately 2 cm square grid that accommodated the taper of the thruster cone. We show these locations in figure 2(d).

4. Analysis methods

In this section, we describe how we use the data resulting from our diagnostic probe measurements to determine both the overall thruster efficiency and the component efficiency modes of equation (4) from section 2.2.

4.1. Estimating per-shot performance metrics

In order to determine of the efficiency of the thruster as outlined in equation (3), we require measurements of the per-shot impulse, energy, and mass. To estimate these, we relate them to steady-state measurements of the thruster operation:

$$J = T/f_{\text{rep}}, \quad (10a)$$

$$M = \dot{m}/f_{\text{rep}} \quad (10b)$$

$$E_{\text{in}} = P_{\text{in}}/f_{\text{rep}}, \quad (10c)$$

where $f_{\text{rep}} = 155$ Hz is the commanded repetition rate of the pulses, T denotes the steady-state thrust measured experimentally over many pulses (>1000), \dot{m} is the constant mass flow rate fed to the thruster, and P_{in} is the average input power to the PPU. The first relationship is justified because the thruster was pulsed at a repetition rate much faster than the natural frequency of the thrust stand. The second equation stems from the fact that the repetition rates were commensurate with the neutral gas fill time (see also section 6.4). The third relationship is based on the fact that although the PPU draws steady power due to passive filtering, power was only consumed by the thruster during the RMF pulse. In addition to these per-shot quantities, we remark here that we determine the specific impulse from our steady-state measurements of thrust and flow rate:

$$I_{sp} = \frac{T}{\dot{m}g_0} = \frac{J}{Mg_0}, \quad (11)$$

where g_0 is the gravitational acceleration at earth's surface.

4.2. Measuring steady-state thrust

We show in figure 3 an example of the measured force from a single thrust measurement. To generate this result, we operate the cathode seed source continuously with a constant propellant flow rate to the thruster and then apply the RMF for a total of ten seconds. We in turn measure the change in thrust-stand displacement caused by the RMF system. We convert the displacement measurement into force via a previously generated calibration against known weights. As can be seen from figure 3, there were large scale oscillations in the measurement due to the under-damped nature of the thrust stand.

In order to estimate thrust from this oscillatory measurement, we calculate an on-delta and an off-delta when the RMF was activated and deactivated respectively. These deltas are determined by taking the average over a three second window on either side of the RMF actuation. We use one standard error over this window to be the uncertainty of the force value. The length of the red bars in figure 3 indicate these averaging windows, and the upper and lower bars correspond to the range of our uncertainty in the mean value. Taking the average value of the two deltas (on and off) and combining their respective uncertainties in quadrature yields a steady thrust value and associated uncertainty for a single measurement. We then repeat three of these trials to capture the variability in the thrust measurement. The final thrust value we report in this work is the average of these three trials, where again the uncertainty is the uncertainties of the individual trials added in quadrature.

4.3. Measuring divergence efficiency

Estimating the divergence efficiency (equation (5)) requires measurements of the ratio of the axially-directed ion

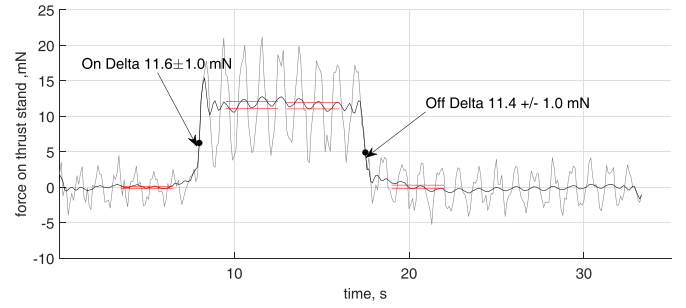


Figure 3. Example thrust measurement with raw thrust data (gray) and a moving average for comparison (black). The red bars indicate the averaging windows of the raw data employed for on/off measurements where the heights indicate the upper and lower values within uncertainty.

momentum compared to the total ion momentum. These values come from measurements integrated over time and space made with the FP of the collected ion current density, j_{FP} , at a radial location r from the thruster as a function of angular position, θ :

$$J_{\text{beam}} = 2\pi r^2 \int_0^{\pi/2} \int_0^{f_{\text{rep}}^{-1}} \phi v dt \sin \theta d\theta, \quad (12)$$

$$J_{\text{axial}} = 2\pi r^2 \int_0^{\pi/2} \int_0^{f_{\text{rep}}^{-1}} \phi v dt \sin \theta \cos \theta d\theta, \quad (13)$$

where $\phi = \frac{m_i j_{\text{FP}}}{Ze}$ is the time-dependent mass flux inferred from measured ion current density, Z denotes average charge state of the ions, and m_i is the ion mass. In the remainder of this work, we assume only singly charged ions are present, and we justify this assumption in section 6. The spatial integral is over the hemisphere normal to the thruster exit plane assuming axisymmetry, while the time integral is over the period of RMF pulsing, f_{rep}^{-1} . The velocity of the particles, v , is explicitly dependent on the time, t , at which they are collected by the probe per the relation:

$$v = r / (t - t_{iz}). \quad (14)$$

Here, t_{iz} is a correction for time delay stemming from the fact that the RMF pulse begins before ionization and plasmoid acceleration. The bounds on this parameter range from $t_{iz} = 0 - 25 \mu\text{s}$, where the latter value corresponds to when density in the thruster reaches half its maximum (see section 5). In the remainder of this work, we calculate the affected parameters (e.g. J_{axial} , J_{beam} , and η_d) over this range of ionization times and use the resulting maximum and minimum values as the effective uncertainty bounds on the estimate with the nominal values coming from $t_{iz} = 12.5 \mu\text{s}$.

We note here that the ion current density as measured with the Faraday probe is related to the raw current by

$$j_{\text{FP}} = \frac{I_{\text{FP}}}{A_{\text{FP}} + \kappa_G} \kappa_{\text{SEE}}, \quad (15)$$

where I_{FP} is the raw signal, A_{FP} is the probe collector area, and κ_{SEE} and κ_G are, respectively, secondary electron emission and

geometric correction factors as presented in [25]. In our case, $\kappa_G = 0.0772 \text{ cm}^2$, or 3.25% of our collector area, and $\kappa_{\text{SEE}} = 97.94\%$ for singly charged xenon striking molybdenum.

4.4. Measuring mass utilization efficiency

To determine the mass utilization efficiency (equation (6)), we require an estimate of the total ion mass flux downstream of the thruster, M_i . To this end, we also employ the FP measurements integrated over the hemispherical surface swept by the probe,

$$M_i = 2\pi r^2 \int_0^{\pi/2} \int_0^{f_{\text{rep}}^{-1}} \phi \, dt \sin \theta \, d\theta. \quad (16)$$

Combining this result with the total injected neutral mass, M , per shot from equation (10b), we can determine mass utilization.

4.5. Measuring coupling efficiency

To motivate an expression for the coupling efficiency (equation (7)) we represent the total energy transmitted by the PPU to the system during a shot as

$$E_{\text{in}} = (R_p + R_c) \int_0^{f_{\text{rep}}^{-1}} (I_x^2 + I_y^2) \, dt, \quad (17)$$

where I_x and I_y are the time-varying currents in the two antennas respectively, and R_p and R_c are the effective resistances arising from the plasma and circuit components respectively. This latter resistance is parasitic, dissipating energy, and leads to a sub-unity coupling efficiency. In this representation, the energy dissipated in the plasma can be written as

$$E_p = R_p \int_0^{f_{\text{rep}}^{-1}} (I_x^2 + I_y^2) \, dt. \quad (18)$$

Combining with equation (17), we thus have for a given RMF shot:

$$\eta_c = 1 - \frac{R_c \int_0^{f_{\text{rep}}^{-1}} (I_x^2 + I_y^2) \, dt}{E_{\text{in}}}. \quad (19)$$

In practice, we measure the total energy imparted into a shot, E_{in} , per the description from equation (10c). We then infer the circuit resistance, R_c , by measuring the impedance of the system during a pulse applied without plasma ($R_p = 0$). We note here that for this analysis we assume that the circuit impedance upstream of the plasma does not change between the vacuum and plasma loaded shots. We in turn assume the plasma is the cause for any changes to the overall circuit impedance from the perspective of the power processing system.

4.6. Measuring plasma efficiency

Lastly, to determine the plasma efficiency (equation (9)), we again employ the measurements of the per-shot quantities, J_{beam} , M_i , and E_p (equations (12), (16) and (18)). As discussed

in section 2.2, we can isolate the various loss terms that contribute to this plasma efficiency including thermal energy, ionization, radiation, and wall losses (equation (8)). These are related to measurements of the beam and local plasma properties through:

$$E_{\text{th}} = 2\pi r^2 \int_0^{\pi/2} \int_0^{f_{\text{rep}}^{-1}} \frac{1}{2} \phi v^2 \, dt \sin \theta \, d\theta - \frac{J_{\text{beam}}^2}{2M_i}, \quad (20a)$$

$$E_{\text{iz}} = \int_0^{f_{\text{rep}}^{-1}} \int_V n_n n_e \langle \sigma_{\text{iz}} v_e \rangle \varepsilon_{\text{iz}} \, dV dt, \quad (20b)$$

$$E_{\text{rad}} = \int_0^{f_{\text{rep}}^{-1}} \int_V n_n n_e \langle \sigma_{\text{ex},n} v_e \rangle \varepsilon_{\text{ex},n} + n_e^2 \langle \sigma_{\text{ex},i} v_e \rangle \varepsilon_{\text{ex},i} \, dV dt, \quad (20c)$$

$$E_{\text{wall}} = \int_0^{f_{\text{rep}}^{-1}} \int_A 0.6 n_e \sqrt{\frac{eT_{eV}}{m_i}} e \left(\frac{5}{2} T_{eV} + 2\Phi \right) \, dA dt. \quad (20d)$$

In the expressions above, n_e is the local plasma density, n_n is the local neutral density, T_{eV} is the electron temperature in electron volts, v_e is the electron thermal speed, A is the inside surface area of the thruster cone, and V is the total volume in the cone.

Equation (20a) uses far-field data from the FP to evaluate the thermal contribution of energy in the ion beam. The first term represents the total integrated kinetic energy of the beam, and the second term subtracts the momentum-carrying component. Equation (20b) represents the loss from the cost of ionization. Here, $\langle \sigma_{\text{iz}} v_e \rangle$ is the reaction rate of ionization averaged over an assumed Maxwellian electron distribution, and $\varepsilon_{\text{iz}} = 12.13 \text{ eV}$ is the first ionization energy for Xe. We again assume here that all the ions are singly charged and each ionization event requires an energy input of ε_{iz} . Next, equation (20c) is essentially a low-fidelity coronal model for radiation, where we assume there is no persistent excited population and that all energy put into the excited states spontaneously radiates out to the environment without re-absorption into the plasma. In this way, we have represented all the excitation processes with an effective total excitation rate and energy per excitation. For the neutral collisions, we adopt the approach from [26], which is informed by [27], in using $\langle \sigma_{\text{ex},n} v_e \rangle$ as the total neutral excitation reaction rate and $\varepsilon_{\text{ex},n} = 8.3 \text{ eV}$ as the average energy per excitation collision. For electron-ion collisions, we have defined $\langle \sigma_{\text{ex},i} v_e \rangle$ as the total ion excitation rate summing for all possible transitions from the ground state, 5p5, to the 6p state. These are the dominant transitions in terms of relative intensity and cross-section [28]. The average energy of these transitions is $\varepsilon_{\text{ex},i} = 14.8 \text{ eV}$. We have plotted these effective reaction rates for neutral and ion excitation averaged over a Maxwellian electron population in figure 4.

Finally, equation (20d) represents the time-integrated power that the electrons and ions carry to the floating thruster wall, where $\sqrt{eT_{eV}/m_i}$ is the Bohm speed and $(5/2T_{eV} + 2\Phi)$ is the energy lost from the plasma per electron/ion pair. Here, $\Phi = T_{eV} \ln \sqrt{2m_i/\pi m_e}$ is the plasma potential with respect to the wall.

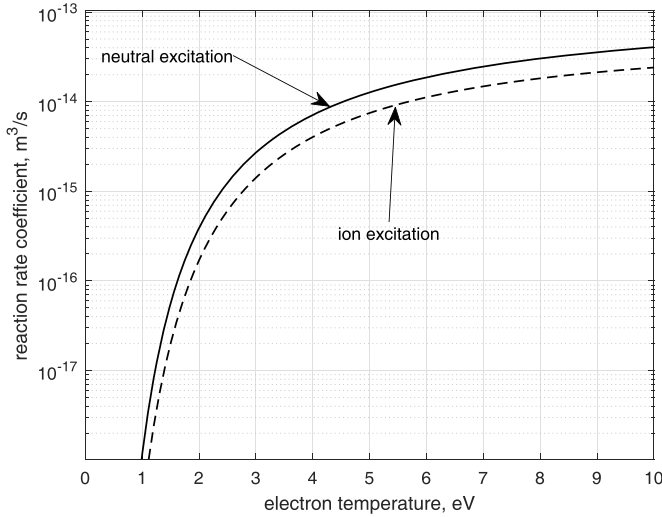


Figure 4. Excitation reaction rates averaged over a Maxwellian electron distribution for neutrals and ions. Neutral excitation rates reproduced from fit from [26]. Ion excitation rates from sum of ground state to 6p transitions from [28].

To evaluate the latter three expressions in equation (20), we require information about the local plasma density, electron temperature, and neutral density. We ascertain the former two from internal spatial measurements based on the raw telemetry from the TLP described in section 3.2. We convert the current and voltage signals from the TLP into density and electron temperature with the following expressions adapted from [29]:

$$1/2 = \frac{1 - \exp(-V_{\text{TLP}}/T_{eV})}{1 - \exp(-V_a/T_{eV})}, \quad (21)$$

$$n_e = \alpha \frac{\pi I_{\text{TLP}}}{eA_p} \sqrt{\frac{m_i}{2e}} \left[\sqrt{V_a - V_{\text{TLP}} + \Phi} - \sqrt{\Phi} \exp\left(\frac{V_{\text{TLP}} - V_a}{T_{eV}}\right) \right]^{-1} \quad (22)$$

where V_{TLP} and V_a are the measured and applied voltage of the TLP respectively, I_{TLP} is the measured TLP current, A_p is the surface area of a single electrode in the probe, and α is an ad hoc scaling factor we introduce. This last parameter is motivated by our assumption for the TLP analysis that the electrons follow a Maxwellian distribution. However, it has been demonstrated that measurements from TLPs in non-equilibrium conditions can lead to errors of up to 50% [30]. In practice, if we do not include this density scaling factor, the experimentally determined plasma energy from the sum in equation (8) is more than twice the energy we measure as coupled into the plasma from equation (18). In our subsequent analysis, we thus adjust this parameter to enforce equal energy in both cases. In practice, this value is within an order of magnitude of unity.

To make an estimate for neutral density, we invoke continuity for the heavy species and make the assumption that convection on the time-scale of ionization is negligible. This is justified by the fact that the neutrals have a much longer transit time compared to the characteristic ionization time-scale, and

our measurements suggest the ions are not accelerated during ionization. We do, however, assume that after the time of peak ionization, effectively all neutrals are converted to plasma. This is supported in section 6.4 by our experimental observation that the mass utilization is of order unity when corrected for wasted gas between shots. We further assume that the plasma density is subsequently governed by convection only. This yields two relations between the neutral density and the plasma density:

$$\frac{\partial}{\partial t} (n_e + n_n) = 0 \text{ for } t \leq t_{pk} \quad (23a)$$

$$\frac{\partial}{\partial t} (n_n) = 0 \text{ for } t > t_{pk}, \quad (23b)$$

where t_{pk} is the time when we measure local peak plasma density. These expressions can be integrated to give an estimate for neutral density at each spatial location:

$$n_n(t) = \begin{cases} n_e(t_{pk}) - n_e(t) & \text{for } t \leq t_{pk} \\ 0 & \text{for } t > t_{pk}. \end{cases} \quad (24)$$

We evaluate the local properties (n_e , n_n , and T_{eV}) at each measurement location from figure 2(d) and perform the integrals in the latter three equations from equation (20) numerically using cylindrical coordinates.

5. Results

In this section, we present the experimental results of the RMF thruster performance and its internal plasma properties. To this end, we first report global performance measurements. Next, we present the raw diagnostic data including: the RMF waveforms measured by the Pearson coils, figures of the FP-measured ion current density, and plots of the average plasma density, electron temperature, and estimated neutral density. Lastly, we report the four phenomenological efficiency values and show how the energy coupled into the plasma is distributed.

5.1. Global performance measurements

In table 1, we show the steady performance values for the RMF thruster including thrust, mass flow rate, and delivered power. We also show the equivalent per-shot values—impulse, mass, and energy—that we inferred from the steady-state measurements per the discussion in section 4.1. Furthermore, we show in this table the calculated specific energy, E_{in}/M , thrust-stand measured thruster efficiency, η (equation (3)), and specific impulse, I_{sp} (equation (11)). The uncertainties in the thrust/impulse values stem from noise, and measurement repeatability as discussed in section 4.2. Mass flow and mass-per-shot errors are inferred from the uncertainty in the mass flow controller. The errors in power and energy readings are related to the uncertainty of the output of the DC power supply, which we conservatively assume to be 5% in both the current and voltage reading.

Table 1. Global performance parameters.

Parameter	Steady value	Per-shot value
Thrust/Impulse	11.6 ± 0.4 mN	74.9 ± 2.5 μ Ns
Mass flow rate/Mass	4.00 ± 0.09 mg s ⁻¹	26.1 ± 0.5 μ g
Power/Energy	4066 ± 287 W	26.2 ± 1.9 J
Specific energy	1.0 ± 0.1 J μ g ⁻¹	
Specific impulse	292 ± 11 s	
Efficiency	$0.41 \pm 0.04\%$	

The values in table 1 are low compared to other state-of-the-art electric propulsion technologies like gridded ion and Hall effect thrusters. The efficiency and specific impulse each are one to two orders of magnitude smaller than typical for those devices. This behavior is commensurate with other RMF thruster research efforts reported to date. For instance, Furukawa *et al* estimated 7 mN of thrust for 3 kW RF power at 1.8 mg s⁻¹ argon flow rate, yielding an efficiency of $\sim 0.5\%$ and a specific impulse of 400 s [31]. These results were for substantially longer RMF pulse lengths (on the order of 100 ms), corresponding to a specific energy per shot of 1.67 J μ g⁻¹. Weber, on the other hand, estimated for the ELF thruster a single-shot impulse of 338 μ Ns for 15.6 μ g of nitrogen, yielding a specific impulse of 2200 s [6]. While this specific impulse exceeds our reported values, this thruster was operated at a minimum of 10 \times the specific energy per shot (J kg⁻¹) of our system at roughly 10 J μ g⁻¹. We note here that the actual total energy per shot (including losses in the driving circuit) was not reported in the previous work by Weber *et al* which precludes a direct comparison with our measurement. With respect to efficiency, Weber in [6] reports a value of 8%; however, this estimate did not include divergence losses, mass utilization, or coupling loss. Allowing for values consistent with our measured contributions (section 5.3), this would bring the ELF efficiency to $<0.7\%$, which ultimately is consistent with our measured efficiency. In light of these low performance metrics, we seek to understand physically what drives these values. For example, the low specific impulse could suggest either purely thermal acceleration and/or low mass utilization. The low efficiency could be attributed to losses driven by any of the mechanisms we identified in section 2.2. We expand upon the causes of these low performance metrics in the following section.

5.2. Diagnostic data

In this section, we present the diagnostic probe measurements from our experiment. This includes the RMF waveform envelopes during vacuum and plasma-loaded operation, the ion current density in the thruster far-field, and the plasma density and electron temperature internal to the thruster volume. We also report on the breakdown of overall thruster efficiency into the efficiency modes identified in section 2.2, as well as the loss contributions of energy coupled to the plasma.

5.2.1. Antenna waveforms. In figure 5, we show the envelopes of the high frequency currents passing through the RMF

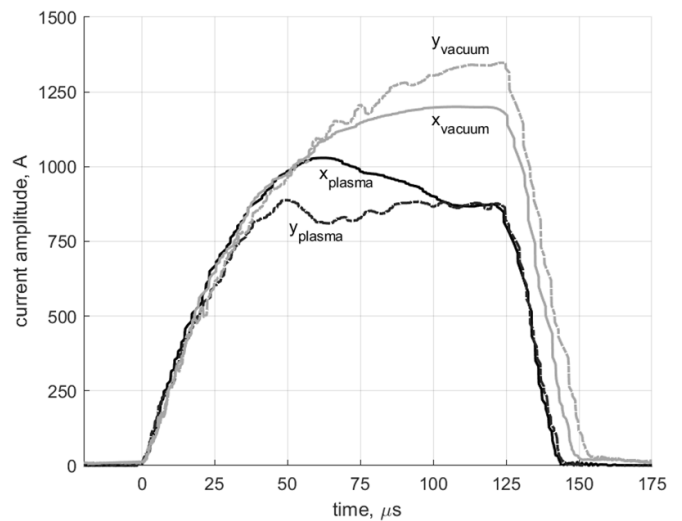


Figure 5. Peak current envelopes through each of the RMF antennas in vacuum and plasma-loaded shots.

antennas for a plasma-loaded and vacuum shot at the same DC input voltage of 235 V. For our RMF PPU operating at resonance, the ultimate value of the current amplitude in each case is determined by the effective resistance of the circuit. The disparity in amplitude between the two antenna sets (denoted X and Y) arises from differing stray inductance, leading to slightly off-resonance operation. For both antennas, the higher peak currents in the unloaded vacuum case are an indication of the overall lower effective resistance in the resonant circuit. The vacuum shot exhibits a monotonic increase during the pulse to a value of 1250 A and the amplitude rapidly decays after the end of the pulse at 125 μ s. For the plasma-loaded case, the initial ramp-up is identical to the vacuum configuration. This physically can be explained by the fact the low-density seed plasma does not present a significant load to the antennas. However, once the remaining propellant is ionized by the increasing RMF-driven current and begins to accelerate, the plasma load becomes significant and leads to the non-monotonic behavior between 50 and 135 μ s. The overall magnitude of the current in the plasma-loaded case reaches a maximum of ~ 1000 A. The difference in area under the two current envelopes (vacuum versus plasma) visually represents the energy coupled to the plasma in the plasma-loaded case.

Leveraging equation (17), we measure an effective resistance for the plasma-loaded case of 282 ± 6 m Ω and an effective resistance of the unloaded vacuum case of 213 ± 1 m Ω . This yields a plasma resistance of 69 ± 6 m Ω . The uncertainty

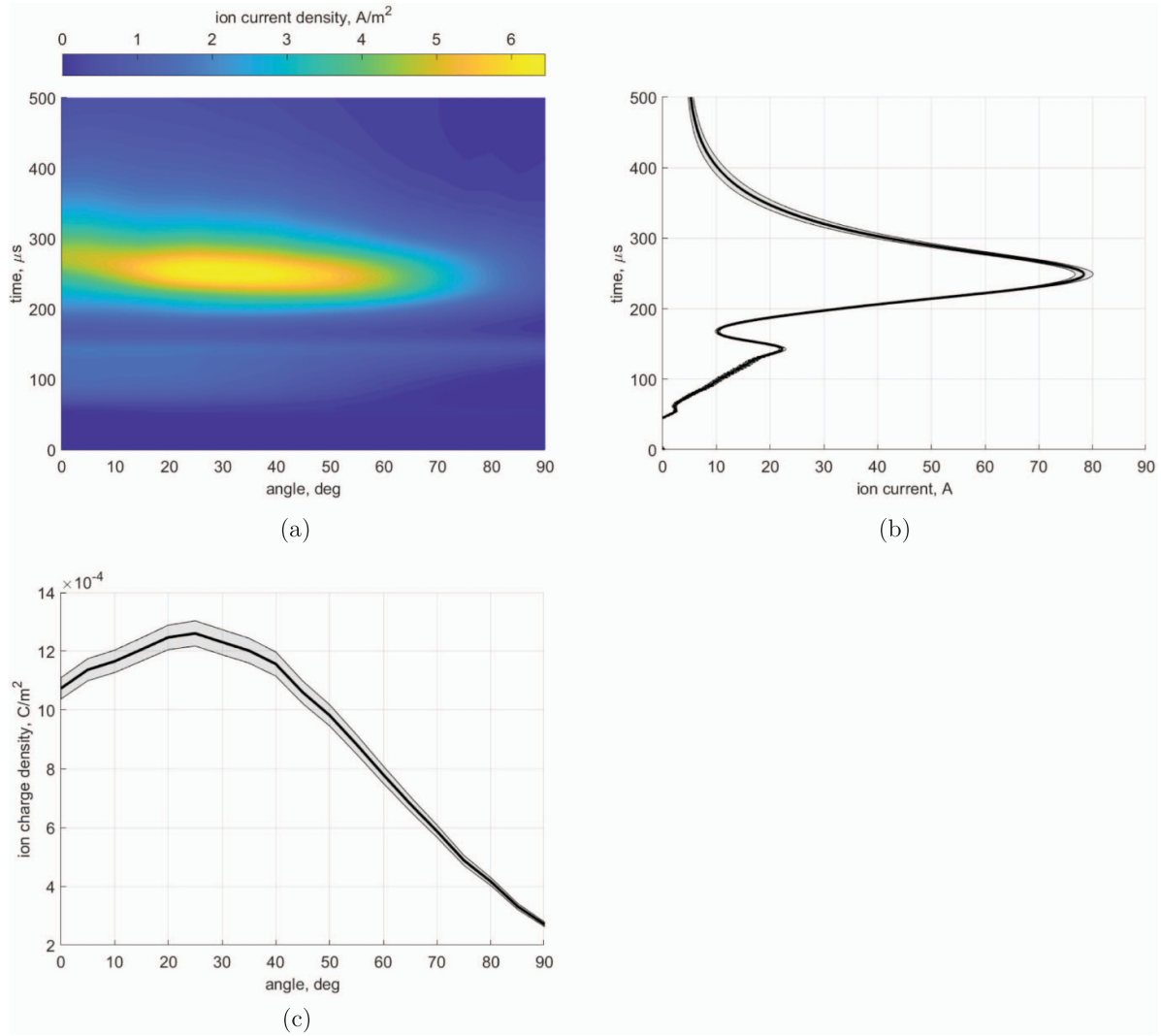


Figure 6. Faraday probe measurements in the thruster far-field at a distance of 1.72 m. Angles are referenced with respect to thruster centerline and the time is referenced with respect to the beginning of the RMF pulse. (a) Ion current density flux, (b) spatially integrated total ion current as a function of time, and (c) temporally integrated ion charge density as a function of angle. Shaded areas indicate the integrated standard deviation over 500 RMF pulses.

in these reported values is the standard deviation over three independent measurements.

5.2.2. Faraday probe current density. In figure 6 we show the measurements made with the FP of ion current density in the thruster plume. Specifically, figure 6(a) shows the full data set as a function of angle and time, where the angles are referenced with respect to thruster centerline. We can further interrogate aspects of the plume acceleration by integrating these results over space or time, which we show in figures 6(b) and (c) respectively.

In figure 6(a), we see a dominant population of ions in the plot at 30° with a time delay of $\sim 250 \mu\text{s}$, exhibited by the maximum in the plot. The peaked structure implies a toroidal plasmoid extending from centerline to 50° . This result can be interpreted as a concentrated population of ions moving at an approximate speed of $u_e = 7 \text{ km s}^{-1}$ away from the thruster

(taking into account the ionization time, $t_{iz} = 12.5 \mu\text{s}$ from section 4). The shape of this population can be attributed to the fact that the majority of RMF-induced current, and by extension Lorentz force acceleration, peaks between the thruster wall and centerline [23]. We remark that the apparent speed of the plasma torus does not directly map to specific impulse, e.g. $I_{sp} \neq u_e/g_0$. This disparity may be explained by large divergence as well as low mass utilization. We discuss the impact of these processes in section 6.2.

We show in figure 6(b) the ion beam current as a function of time. In this form, the ion current exhibits a notable dispersion with a tail that extends beyond $500 \mu\text{s}$. The results in figure 6(b) suggest that although the bulk of the plasma is accelerated to the same speed, the RMF scheme results in a continuous spectrum of ion velocities. There may be a few factors driving this effect. For example, while the Lorentz force acts across the bulk of the thruster, ions at the back of the device will experience a longer exposure to this body force,

thereby gaining more acceleration. The spatial distribution of ions subject to acceleration thus may result in a spectrum. Similarly, the spread may also be attributed to the influence of other forces in addition to the axial Lorentz force. For example, ions may be heated by compression from the radial component of the Lorentz force. Additionally, we note the existence of an early peak in current density between 75 and 150 μs , which is plausibly explained by the existence of faster, doubly-charged Xe^{2+} . We cannot explicitly confirm this, however, as we did not measure the ion charge state as a function of time in this work. For simplicity, in the remainder of our analysis (equations (12), (13), and (16)), we ultimately neglect the contribution of any such secondary population. Given the low current density associated with this higher velocity population, we have found this simplification at most results in an error of 3% from our reported values.

We next show in figure 6(c) the FP-measured current density integrated over time. This results in a plot of charge density as a function of angle with respect to the thruster centerline. The large characteristic divergence of the RMF is evident from this plot, with substantial charge density extending out to an angle of 50° . Furthermore, the dip in charge density on centerline is consistent with our interpretation of a toroidal structure.

As figures of merit, we can use the data presented in figure 6 combined with equations (12)–(16) to determine key aggregate values for mass and momentum. To this end, we find the resulting cumulative ion mass, $M_i = 20.06 \pm 0.07 \mu\text{g}$, the total beam impulse, $J_{\text{beam}} = 128 \pm 10 \mu\text{Ns}$, and the axial component of the impulse, $J_{\text{axial}} = 82 \pm 7 \mu\text{Ns}$. Here, the errors stem from the propagation of the standard deviation of our 500 FP traces at each angular position and the uncertainty in our assumption of the ionization time delay.

5.2.3. Triple Langmuir probe plasma properties. In figure 7 we show the spatially averaged properties of the plasma discharge from the TLP as a function of time. As discussed in section 3.2, we generated these plots by translating the probes within the thruster between shot bursts and using the repeatability of the shots to synchronize measurements. The results shown here are averaged by performing a numerical integral of the local plasma properties over the internal thruster volume in cylindrical coordinates. We have chosen to present the spatial averages in figure 7 as the trends in the local parameters are generally global. The scaling factor we have employed (per equation (22)) for determining the density from the raw TLP trace is $\alpha = 0.637$. We also show in figure 7 the estimated volume-averaged neutral density from equation (24). We note that the uncertainty reported in these results is assumed to be a flat 50% for both density and temperature. As we discussed in section 4, Langmuir probes and TLPs in particular are known to be inaccurate in non-equilibrium conditions up to our assumed degree of error, which is beyond what can be accounted for statistically [30, 32].

The mean plasma density begins to increase rapidly at the beginning of the RMF pulse and peaks at $1.9 \times 10^{19} \text{ m}^{-3}$ after 50 μs . We take the time that the plasma density reaches half of this maximum (25 μs) as the upper bound

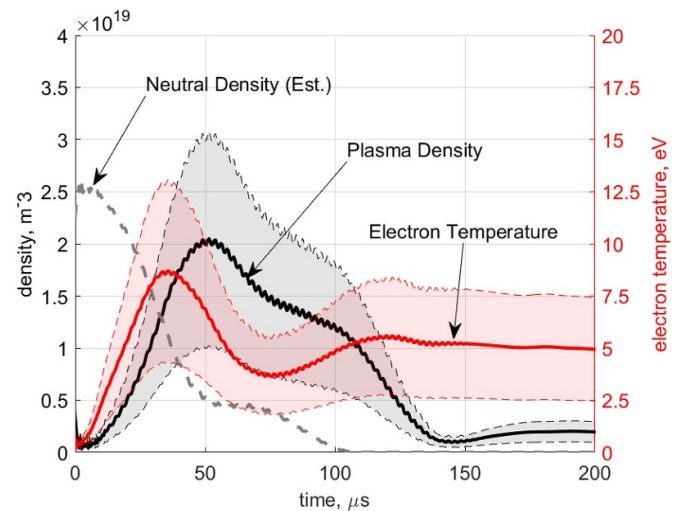


Figure 7. Spatial average of plasma density (black) and electron temperature (red) as measured by the TLP. Gray dashed line indicates estimate of neutral density for loss calculations. $\alpha = 0.637$ is the scaling factor from equation (22).

on possible ionization delay times, t_{iz} , for the calculation of probe-measured impulse in equations (12) and (13). Following this peak, the plasma density decays for the duration of the plasma shot. This is a qualitative indication of the acceleration of the plasma out of the geometry.

The electron temperature as shown in figure 7 also increases with the RMF pulse duration. Notably, the peak electron temperature is less than the first ionization energy of xenon (12.1 eV), indicating that the bulk of our electrons do not have sufficient energy for ionization. This suggests the high rates of ionization we observe likely is driven by a high energy electron tail in the electron energy distribution. Relatedly, we suspect that there may be an even higher energy population contributing to the formation of doubly charged ions. While we were not able to resolve such a population with our triple probing scheme, the fact that we needed to bias the Faraday probe to such high negative potentials (section 4) suggests indirectly that tail electrons may be present. The electron temperature profile leads the density by approximately 12 μs . The evolution of the average temperature with time profile likely can be explained by a balance between Ohmic heating from the RMF and energy sinks—such as ionization, wall loss, and radiation—that are linked to the evolving plasma density.

5.3. Efficiency breakdown

With our plasma diagnostic results, we can calculate and compare our efficiency terms as defined in section 2.2. We show these values in figure 8, where we also plot for comparison the efficiency as inferred from the thrust stand, η_{TS} , as well as the product of the terms inferred from probing, η_{probe} . We found the divergence efficiency shown in this result by comparing the total beam impulse to the axially directed impulse. This yielded $\eta_d = 40.2 \pm 0.2\%$ with a characteristic divergence angle of $\Theta \approx 50^\circ$. This angle is consistent with the spatial distribution exhibited by figure 6(c). We calculated the

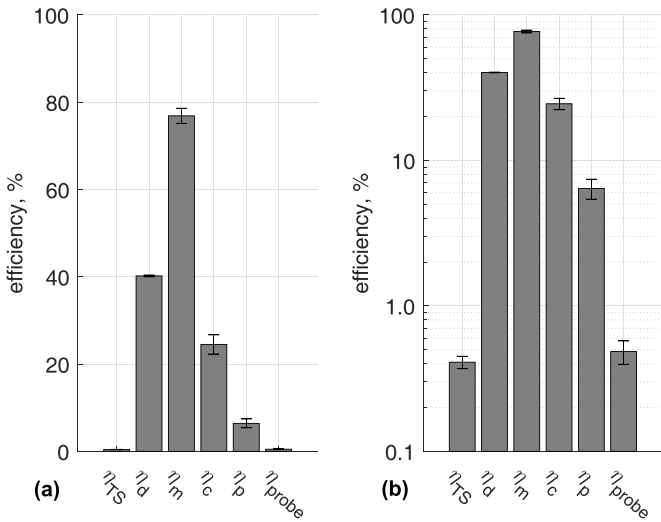


Figure 8. Breakdown of phenomenological efficiencies compared to total thrust stand measured efficiency. (a) Linear scale, and (b) log scale for clarity.

mass utilization from the measured total ion mass and the neutral mass per shot to arrive at a value of $\eta_m = 76.9 \pm 1.7\%$. Using the effective circuit resistances from the vacuum and plasma-loaded PPU, we determined a coupling efficiency of $\eta_c = 24.5 \pm 2.2\%$. Finally, with the beam impulse, ion mass, and plasma coupled energy, we calculated a plasma efficiency of $\eta_p = 6.4 \pm 1.0\%$. The product of these terms gives us a probe-measured efficiency of $\eta_{probe} = 0.49 \pm 0.09\%$.

We see that overall the probe-measured efficiency agrees with the thrust stand efficiency within uncertainty. Furthermore, we note here that all of our terms are low when compared to equivalent terms in phenomenological efficiency analyses of more conventional electric propulsion systems like gridded ion and Hall effect thrusters. This is to be expected given that the overall performance of the RMF system is also lower.

While we discuss the physics impacting the magnitude of each efficiency mode in more detail in section 6, we briefly comment here on key trends. Specifically, the mass utilization is large relative to the other modes indicating a high degree of conversion of neutral gas to plasma. The low divergence efficiency reflects the low collimation of the plume. The small coupling efficiency indicates 75% of the energy is parasitically consumed by the PPU and RMF antennas. Finally, the low plasma efficiency, which is the major driver for poor performance, suggests that 94% of the energy successfully coupled into the plasma by the RMF is not successfully converted to thrust.

5.4. Plasma energy breakdown

We expand here on the key factors that influence the plasma efficiency, η_p , which as we found in the previous section is the dominant loss mechanism for the RMF thruster. To this end, we show graphically in figure 9 the five channels of plasma energy from equation (8). As can be seen, the impulsive energy

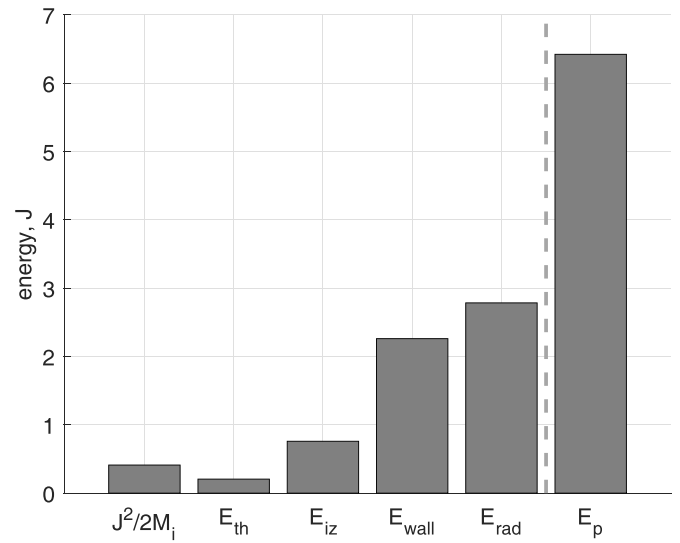


Figure 9. Energy distributed by channel compared to total coupled energy. E_p is equivalent to the sum of the first five bars and the coupled plasma energy from equation (18).

to the plasma, $J^2/2M_i$, which represents the energy successfully converted to thrust, is the second lowest term. This is consistent with the observation that overall plasma efficiency is low. The second bar represents the thermal energy of the ions. This is the smallest energy mode, but it is significant relative to the impulsive energy. The relatively high degree of thermal energy may be explained either by variations in the magnitude of the accelerating force acting on the plasma—due to charge state or the radial dependence of axial Lorentz force—or by compressive work done by the radial component of the Lorentz force ($j_\theta \times B_z$). The ionization loss presented in figure 9 represents the energy expended from the total rate of ionization collisions (from equation (20b)). This power/energy is four times larger than the minimum ‘frozen flow’ ionization cost based on the ejected ion mass ($E_{iz}^{frozen\ flow} = \varepsilon_{iz} M_i / m_i$). This discrepancy might be attributed to high re-combination rates that stem from the high plasma densities in the device. The wall loss as shown in figure 9 is four times greater than the impulse energy. Thus, this also represents a substantial loss to the plasma efficiency and likely can be explained by poor magnetic confinement of the electrons. Finally, optical radiated energy out of the thruster is the largest loss. This radiation is primarily caused by the n_e^2 scaling of electron-ion excitation collisions, which dominate for the atypically large average plasma densities (compared to Hall or gridded thrusters, for example) exhibited during RMF pulsing. This idea of radiation losses being dominant for RMF thrusters has been indicated previously by Weber [6] and has also been suggested as an efficiency limiter for PIT thrusters by Polzin *et al* [33].

In summary, we have shown that the performance of our RMF test article is consistent with previously reported experimental results, with an overall thrust efficiency of $0.41 \pm 0.4\%$ and a specific impulse of 292 s. Leveraging our phenomenological efficiency breakdown, we in turn have demonstrated that this poor performance can primarily be attributed to a

low plasma efficiency, $\eta_p = 6.4 \pm 1.0\%$. This indicated that very little of the energy put into the plasma is converted to usable directed kinetic energy. Further examination into the energetic processes within the plasma revealed that the plasma loses energy during the formation process primarily to excitation radiation and losses to the thruster walls. In the following section, we expand on the implications of these results and leverage our findings into possible strategies for improving performance.

6. Discussion

In this section, we discuss limitations of our experimental methods and analysis. Additionally, we attempt to motivate physics-based explanations for the low performance of the RMF thruster. We in turn suggest possible strategies, informed by our measurements, for increasing efficiency.

6.1. Experimental limitations

We address here the validity of the key simplifying assumptions we have made in this study. As a first consideration, the time-of-flight velocimetry of the ion beam has a degree of ambiguity from the selection of an ionization time delay, t_{iz} . In this work, we chose the upper bound of t_{iz} such that it corresponded to the time that the measured plasma density reached half its peak value. This is a physically plausible criterion based on the interpretation that the plasma will not accelerate until achieving a critical density. In practice, we were not able to directly measure the ion transit time as we did not have direct velocity or energy information of the ion beam. Ultimately, we chose a sufficient range of t_{iz} to capture the uncertainty of our assumption, and this error is reflected in our reported values. To improve the accuracy of the ion speed measurement, future work could include a near-field trigger probe to set a zero-drift-time reference or employ direct methods for ion velocimetry like laser induced fluorescence.

Secondly, we have remarked in the preceding that the existence of non-equilibrium electrons may lead to errors in the TLP measurements [30]. With that said, we can estimate the relaxation time, i.e. the equilibrium time, of fast electrons from the energy transfer collision frequency to be on the order of 40 ns [34]. This is much faster than the RMF pulse length, thus providing credibility to our assumption of electron thermal equilibrium. With that said, the electron drifts caused by the RMF may sustain a high energy tail in the electron energy distribution. This could explain why it was necessary to invoke a correction factor (section 4.6) to give physically plausible plasma densities, as TLPs tend to over-measure density and under-measure electron temperature in non-equilibrium conditions [30].

Lastly, for our analysis of plasma efficiency, when we calculated the energy sub-terms we made two major simplifications. First, we assumed the plasma freely streamed to the walls at the Bohm speed. However, the actual near-wall plasma in the thruster is subject to the applied magnetic field as well as fields arising from the RMF and azimuthally driven

electron currents. In practice, we anticipate this combination of fields likely provides some enhanced electron confinement in our thruster. Given this simplification, we would expect that our estimated ion current to the walls is an overestimate. Our reported value for wall loss is consequently an upper bound. Second, our estimates of radiative loss do not incorporate a detailed collisional model for xenon. For simplicity, we instead opted to represent the energetic loss due to the most prevalent excitation transitions for neutrals and singly charged ions. Similarly, equation (20c) does not include any mechanism for photon absorption or collisional de-excitation, which can be important factors for total emitted radiation at or above our measured plasma densities [35]. We anticipate that neglecting these effects may ultimately translate to an under-prediction for the actual radiation losses. Our reported value thus represents a lower bound.

In practice, we have attempted to include large yet physical error bounds to represent the culmination of these effects. To this point, even when we do allow for these relatively large uncertainties, our overall conclusions remain unchanged. For example, a key finding that we have found to hold outside of error bars is that radiation losses dominate the low plasma efficiency.

6.2. Specific impulse

As we noted in section 5.2, the effective ion exhaust velocity based on the thrust-stand measured specific impulse was lower than the time-of-flight ion velocities we measured. In particular, the bulk ion speed as measured by the FP was $\sim 7 \text{ km s}^{-1}$, which should correspond to a specific impulse of $I_{sp} \approx 700 \text{ s}$. We can explain this discrepancy, however, if we account for the divergence and mass utilization efficiencies. Taking these efficiency values into account leads to an effective $I_{sp} = 218 \text{ s}$ from ion velocity measurements, which has better agreement to the thrust-stand measured specific impulse of $I_{sp} = 292 \pm 11 \text{ s}$.

Even though we can reconcile these measurements, we would still expect the effective specific impulse to be higher for an electromagnetic accelerator such as the RMF thruster. To further analyze the causes underlying this low specific impulse, we can separate the measured beam impulse, J_{beam} , into terms relating to the Lorentz and thermal acceleration of the plasma:

$$J_{\text{beam}} \approx \int_0^{f_{\text{rep}}^{-1}} \left[\int_{\partial V} j_{\theta} B_r dV + \langle n_e e T_{eV} \rangle A_{\text{exit}} \right] dt, \quad (25)$$

where the first term is the integral over the internal thruster volume of the product of azimuthal current density j_{θ} and the radial magnetic field B_r . The second term in equation (25) results from the product of the volume averaged electron thermal pressure force and the exit area A_{exit} . The measurement of j_{θ} and B_r is the subject of a companion work [23] and for brevity is not reproduced here.

We plot the two terms from equation (25) in figure 10. From the figure, we can see that the pressure force vastly dominates over the Lorentz force. Correspondingly, in time-integrated

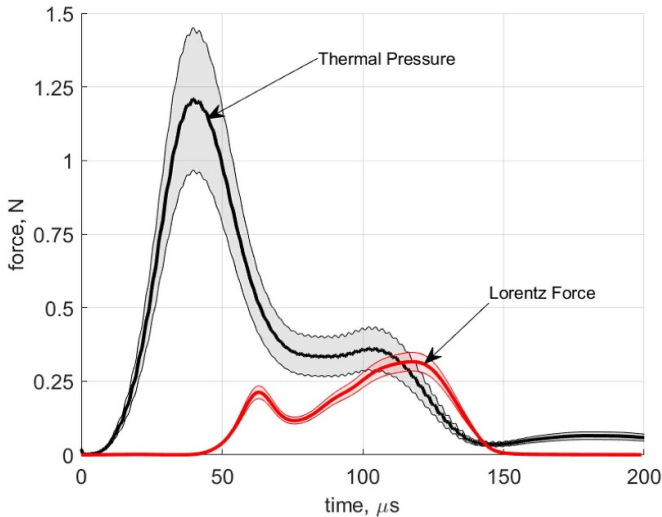


Figure 10. Internal axial forces: thermal electron pressure and axial $j_{\theta} \times B_r$ Lorentz force.

quantities, the thermal impulse is $83 \pm 23 \mu\text{Ns}$ and the Lorentz impulse is $18.8 \pm 1.9 \mu\text{Ns}$, less than a quarter of the thermal term. Given that the thermal force is dominant, it is unsurprising that the thrust stand measured specific impulse of the thruster is low (<300 s).

Undoubtedly, this low specific impulse is a symptom of the low efficiency of the RMF thruster and the losses that occur during plasma formation, as the thruster is designed to operate as an electromagnetic accelerator and not via electron thermal pressure. In the remainder of this discussion, we turn to the individual phenomenological efficiency terms to interpret our measured results and propose solutions to address thruster performance.

6.3. Divergence efficiency

The low divergence efficiency for the RMF thruster is a physical indication that the plume is not well-collimated. This large divergence is likely a combination of the sharply diverging magnetic bias field in this region [19], and the dominance of thermally-produced isotropic thrust. It is interesting to note that electron cyclotron resonance thrusters—which employ a similar accelerating magnetic nozzle to an RMF thruster—experimentally exhibit a tighter and more axial beam, with divergence efficiencies between 85% and 90% [21]. This suggests that the divergence of our test article may be improved. One such method may be to provide a stronger axial component of the bias field as this ideally would provide a compressive force when reacted with the driven azimuthal current. We do note, however, that a more axial applied magnetic field may adversely impact Lorentz-force acceleration, as the radial component of magnetic field would necessarily be reduced for a fixed field strength. An additional potential result of this could be increased ion heating due to higher compression leading to increased divergence from randomized thermal motion. Ultimately, we believe careful investigation into the optimum shape of the magnetic field such that the electron dynamics

promote axial ion motion is necessary to better collimate the plasma to improve divergence efficiency.

6.4. Mass utilization

The mass utilization efficiencies measured in this experiment are not the critical loss factor to overall thruster performance. This is a notable contrast to previous computational work [11], where it was indicated that mass utilization could contribute a significant efficiency loss for RMF thrusters due to the interaction of a propagating ionization front with dense downstream neutrals. We intuit that the high mass utilization found in this experiment occurs from the high plasma densities resulting from the large amplitude current transients. This is further evidenced by the large power sink to—and therefore rate of—ionization estimated in section 5.4.

We remark that the mass utilization is not unity primarily because of wasted gas between shots. To illustrate, we can define an estimate for the available neutral mass for a pulse using

$$M_{\text{fill}} = \frac{4\pi L}{c_{\text{th}}}, \quad (26)$$

where L is the thruster length and c_{th} is the neutral thermal speed. In this work, this fill mass is $20.2 \mu\text{g}$. Compared to the ion mass from equation (16), this indicates an effective mass utilization of 99.3% for a given pulse. This implies that the thruster utilizes nearly all of the gas that is present when a shot is performed.

Therefore, in order to increase mass utilization, we could in principle increase the pulse rate such that the fill time is commensurate with the pulse rate. For example, we can estimate a fill time for our test article of $t_{\text{fill}} = 4L/c_{\text{th}}$. This value suggests that the optimal pulse repetition frequency for our thruster is ~ 200 Hz (in contrast to our rate of 155 Hz). While we did not explore this dependency rigorously in this effort, this is another potential strategy for marginally increasing thruster performance.

6.5. Coupling efficiency

Our measured values for coupling efficiency ($\sim 25\%$) indicate physically that only this small fraction of energy delivered from the power supply reaches the plasma. There are two main sources of parasitic loss driving this: resistance in the antennas and resistance in the driving elements from the PPU. To evaluate the contributions from the former, we can make an estimate for the resistance of only the antennas by assuming a $2\times$ characteristic skin depth at 415 kHz. The estimated combined resistance for the two antennas of $21.6 \text{ m}\Omega$. Comparing this antenna resistance to our measured plasma resistance (similar to section 5.2), we find that a substantial portion of the power input to the antennas, 76%, is coupled to the plasma. This indicates an efficient power transfer to the plasma from the antennas and is commensurate with the calculated antenna-only coupling efficiency of the ELF thruster [6]. This suggests the overall coupling losses are dominated by the energy absorbed by the switching circuit of our PPU.

Potential solutions to mitigate coupling loss include increasing the load of the plasma or decreasing the resistance of the circuit. Addressing the first point, the startup process of pulsed operation leads to a substantial period when little plasma is present to absorb energy. This suggests that longer pulses of the RMF thruster could lead to higher coupling efficiency by not incurring this startup loss for a given duty cycle as frequently. Additionally, increasing plasma density via higher flow rate could also increase the effective plasma load. We note, however, that the gains in coupling efficiency from this latter process may be offset by the reduction in plasma efficiency produced from higher plasma density (section 5.4). Finally, lack of a uniform RMF field has been numerically demonstrated to adversely affect the plasma current drive—and by extension plasma loading—in RMF plasma systems [36]. These findings show that additional antenna phases can work to increase RMF uniformity by reducing the impact of anti-rotational harmonics in the system, and therefore may help improve RMF thruster coupling.

With respect to the second mitigation strategy, the resistance in the PPU circuit could be reduced by lowering the overall current delivered through the RMF antennas. This stems from the fact that the switching losses for the solid state IGBTs in the PPU are roughly linear with the driven antenna current. With that said, this reduction in current will also result in decreased RMF penetration into the plasma column for a fixed electron density, leading to a reduction in the driven azimuthal current and by extension Lorentz force. This process in turn may be mitigated through the use of multiple-turn antennas to increase the magnetic flux for a given current.

In practice, there are several avenues to address low coupling efficiency and many of these trade at the expense of reducing other efficiency terms. Ultimately, while our test article was not optimized to maximize coupling efficiency, these insights may prove beneficial to increasing coupling in future efforts.

6.6. Plasma efficiency

As shown in section 5.3, the plasma efficiency (figure 8) is the dominant loss in the thruster. We further evaluated the loss components to plasma efficiency (figure 9) to better understand the plasma formation process. From these results our general conclusion is that the dominant loss processes in plasma efficiency are those that scale most with plasma density—linearly in the case of wall losses and quadratically for radiative losses. The dominance of radiative loss in particular arises from the unusually high density in the RMF thruster. Indeed, peak density shown in figure 7 is a factor of 10 higher than the peak plasma density exhibited in a 5 kW class Hall thruster operating at more than twice the propellant flow rate [37] and a factor of 100 higher than the density exhibited in a 5 kW class gridded ion thruster [38] at a similar flow rate. This higher density in the RMF system, coupled with the fact that the peak densities in the RMF are spatially global over several centimeters—as opposed to spatially localized over a few millimeters as is the case with Hall

and gridded ion thrusters—explains why radiative excitation is a comparatively larger loss for this thruster.

The root cause of this high density may be in fact the pulsed operation of the thruster. Prior to RMF activation, a slow-moving, dense neutral gas fills the volume. These dense neutrals then quickly become ionized by the RMF as evidenced by our results in figure 7 to form a correspondingly dense plasma. As a potential solution to this problem, we recently have examined the advantages of operating the thruster in a continuous wave (CW) mode of operation rather than pulsed [39]. In this mode, we posit neutral gas would not be able to build up to the same level as in a pulsed mode because propellant would be continuously extracted in the ion beam at a velocity higher than the neutral thermal speed. As a first order assessment of this concept, we attempted to predict in [39] the performance of a CW mode thruster by extrapolating internal plasma measurements of density and current drive at the end of long (~ 1 ms) pulses from our RMF test article [39]. These results indicated there may be modest improvements for a CW mode thruster, though we emphasize that at this point, the advantages of CW mode are largely speculative. Further experimental efforts are required to evaluate these claims.

With that said, even provided we can reduce the radiative and thermal losses, the energy analysis revealed by figure 9 suggests the thruster performance may still be low. This stems from the fact that the acceleration energy is less than the ionization energy—the minimal frozen flow loss with the device. Indeed, based on these values, the result may suggest that the maximum efficiency would be 30%–40%. In practice, the reason for this upper bound bound likely can be attributed to poor acceleration in the thruster—suggesting that the Lorentz acceleration is low. To this point, in our recent work [23], we experimentally investigated the acceleration dynamics in the thruster and showed that the Lorentz force is modest compared to thermal effects. This result does not necessarily suggest that this is an inherent limitation of the thruster, however, as we have only examined in detail the one operating condition reported here. As discussed in this other work, there are strategies based to manipulating the density, RMF power conditioning, and bias field geometry that ultimately may help enhance the acceleration.

7. Conclusion

In this work, we have experimentally investigated the reasons for the low efficiencies historically exhibited by RMF thrusters. To this end, we established a phenomenological efficiency model for RMF thrusters consisting of four terms: divergence efficiency, mass utilization, coupling efficiency, and plasma efficiency. We then performed a suite of plasma diagnostic measurements to individually evaluate each term's contribution to overall thruster efficiency. Our results indicated a divergence efficiency of $40.2 \pm 0.2\%$, a mass utilization of $76.9 \pm 1.7\%$, a coupling efficiency of $24.5 \pm 2.2\%$ and a plasma efficiency of $6.4 \pm 1.0\%$. These results combined led to a probe-measured efficiency of $0.49 \pm 0.09\%$, which is

in close agreement to the thrust stand measured efficiency of $0.41 \pm 0.04\%$.

This efficiency measurement agrees in order of magnitude with the results from previous experimental studies of RMF thrusters (See the discussion in section 5.1). However, it is markedly below the theoretical value of 85% anticipated from previous analytical studies [5]. With that said, an examination of this previous theoretical treatment shows that the analysis neglected the contributions of wall, recombination/ionization, and radiative losses. As our work has shown, these can be dominant drivers for performance loss. Indeed, our analysis suggests that the majority of the energy lost from the plasma is in the form of electromagnetic radiation due to excitation collisions in the plasma. These radiative losses are the result of high plasma densities that occur in the RMF pulse, which reach values greater than $1 \times 10^{19} \text{ m}^{-3}$. The magnitude of these loss modes suggests that the estimates for actual theoretical upper bound in performance may need to be revisited.

To this end, we have discussed the physical drivers of each efficiency mode and leveraged our results to propose strategies to reduce their detrimental effects. A major conclusion from our work is that the shortcomings of the current version of the RMF thruster stems from the high densities inherent to pulsed-mode thrusters. Indeed, RMF thrusters are a departure from more conventional PITs where the coupling between high amplitude, transiently-induced currents interacts with the high amplitude induced magnetic field to yield quadratic scaling with the applied current. The corresponding high thrust density in these devices presumably overcomes radiative and wall losses characteristic of high plasma density. By design, however, the RMF current drive scheme avoids high amplitude, transiently-induced currents to enable low voltage operation (see section 1). This minimizes quadratic scaling with applied current in favor of an acceleration process depends on a linear interaction between the amplified current and background magnetic field [18]. As result, the high densities associated with pulsed operation serve only to adversely impact RMF thruster efficiency. This finding would suggest that pulsed-mode RMF thrusters may be unable to achieve the efficiency levels competitive with state-of-the-art pulsed inductive and steady-state electric propulsion devices. With that said, there may be other methods for leveraging RMF for accelerating plasmas, such as using RMF in a continuous mode rather than pulsed, that may avoid the problem of prohibitively high radiative losses. This is an area for future investigation.

In summary, our findings here have provided critical insights into the present operation and future development of this low maturity but still promising technology. We anticipate that these results may be leveraged to realize the full potential of RMF thrusters.

Data availability statement

The data collected for this work is publicly available at Deep Blue Data (<https://doi.org/10.7302/2g14-pg75>).

Acknowledgments

We would like to thank Eagle Harbor Technologies for their development of the RMF power processing unit and their technical support. Furthermore, we would like acknowledge the sponsors of this work. Funding was supplied under an AFOSR Grant FA9550-19-1-0022 from the Space Propulsion and Power portfolio, NSTGRO Fellowship Grant Number 80NSSC20K1168, and NSTRF Fellowship Grant Number 80NSSC18K1190.

ORCID iDs

T M Gill  <https://orcid.org/0000-0002-5585-4869>
 C L Sercel  <https://orcid.org/0009-0006-5374-4689>
 B A Jorns  <https://orcid.org/0000-0001-9296-2044>

References

- [1] Polzin K, Martin A, Little J, Promislow C, Jorns B and Woods J 2020 *Aerospace* **7** 105
- [2] Rovey J L, Lyne C T, Mundahl A J, Rasmont N, Glascock M S, Wainwright M J and Berg S P 2020 *Prog. Aerosp. Sci.* **118** 100627
- [3] Mikellides P G and Villarreal J K 2007 *J. Appl. Phys.* **102** 103301
- [4] Polzin K A 2011 *J. Propuls. Power* **27** 513–31
- [5] Slough J T, Kirtley D E and Weber T E 2009 *31st Int. Electric Propulsion Conf.*
- [6] Weber T E 2010 The electrodeless Lorentz force thruster experiment PhD *Thesis* University of Washington
- [7] Kirtley D E, Slough J T, Pfaff M and Pihl C 2011 *Joint Army Navy NASA AirForce Conf.*
- [8] Waldock J, Kirtley D E and Slough J T 2013 *33rd Int. Electric Propulsion Conf.*
- [9] Furukawa T, Shimura K, Kuwahara D and Shinohara S 2019 *Phys. Plasmas* **26** 033505
- [10] Furukawa T, Shinohara S and Kuwahara D 2020 *AIAA Propulsion Energy Forum* (<https://doi.org/10.2514/6.2020-3630>)
- [11] Brackbill J, Cambier J L, Gimelshein N E and Gimelshein S F 2014 *J. Propuls. Power* **30** 1450–8
- [12] Liang R and Gallimore A D 2011 *49th AIAA Aerospace Sciences Meeting Including the New Horizons Forum and Aerospace Exposition* (<https://doi.org/10.2514/6.2011-1016>)
- [13] Hofer R R and Gallimore A D 2006 *J. Propuls. Power* **22** 732–40
- [14] Linnell J A and Gallimore A D 2006 *J. Propuls. Power* **22** 1402–12
- [15] Jones I R and Hugrass W N 1981 *J. Plasma Phys.* **26** 441–53
- [16] Mikellides P G 2003 *28th Int. Electric Propulsion Conf.*
- [17] Sercel C L, Gill T M and Jorns B A 2022 *37th Int. Electric Propulsion Conf.*
- [18] Sercel C L, Woods J M, Gill T M and Jorns B A 2020 *AIAA Propulsion and Energy Forum* (<https://doi.org/10.2514/6.2020-3632>)
- [19] Sercel C L, Gill T M, Woods J M and Jorns B A 2021 *AIAA Propulsion and Energy Forum* (<https://doi.org/10.2514/6.2021-3384>)
- [20] Miller K E, Prager J, Henson A, McEleney K, Woods J, Sercel C, Gill T, Viges E and Jorns B 2021 *IEEE Int. Conf. on Plasma Science* (<https://doi.org/10.1109/ICOPS36761.2021.9588361>)

- [21] Correyero S, Jarrige J, Packan D and Ahedo E 2019 *Plasma Sources Sci. Technol.* **28** 095004
- [22] Chen S L and Sekiguchi T 1965 *J. Appl. Phys.* **36** 2363–75
- [23] Sercel C L, Gill T M and Jorns B A 2023 *Plasma Sources Sci. Technol.* **32** 105017
- [24] Dankanich J W, Walker M L R, Swiatek M W and Yim J T 2017 *J. Propuls. Power* **33** 668–80
- [25] Brown D L, Walker M L R, Szabo J, Huang W and Foster J E 2017 *J. Propuls. Power* **33** 582–613
- [26] Goebel D M and Katz I 2008 *Fundamentals of Electric Propulsion: Ion and Hall Thrusters* (Jet Propulsion Laboratory, California Institute of Technology) (<https://doi.org/10.1002/9780470436448>)
- [27] Hayashi M 1983 *J. Phys. D: Appl. Phys.* **16** 581–9
- [28] Wang Y, Wang Y F, Zhu X M, Zatsarinny O and Bartschat K 2019 *Plasma Sources Sci. Technol.* **28** 105004
- [29] Gill T M, Sercel C L, Woods J M and Jorns B A 2022 *AIAA Science and Technology Forum* (<https://doi.org/10.2514/6.2022-2191>)
- [30] Polzin K A, Blumhagen E, Sherrod A C and Moeller T M 2019 *AIAA Propulsion and Energy Forum* (<https://doi.org/10.2514/6.2019-3990>)
- [31] Furukawa T, Takizawa K, Yano K, Kuwahara D and Shinohara S 2018 *Rev. Sci. Instrum.* **89** 043505
- [32] Lobbia R B and Beal B E 2017 *J. Propuls. Power* **33** 566–81
- [33] Polzin K A, Martin A K, Eskridge R H, Kimberlin A C, Addona B M, Devineni A P, Dugal-Whitehead N R and Hallock A K 2013 *Summary of the 2012 Inductive Pulsed Plasma Thruster Development and Testing Program* (NASA-Marshall Space Flight Center)
- [34] Huba J D 1998 *NRL Plasma Formulary* vol 6790 (Naval Research Laboratory)
- [35] Celik M 2007 Experimental and computational studies of electric thruster plasma radiation emission PhD Thesis Massachusetts Institute of Technology (<https://doi.org/1721.1/40306>)
- [36] Hugrass W N 1982 *J. Plasma Phys.* **28** 369–78
- [37] Haas J and Gallimore A 2000 An investigation of internal ion number density and electron temperature profiles in a laboratory-model hall thruster *36th AIAA/ASME/SAE/ASEE Joint Propulsion Conference and Exhibit* p 3422
- [38] Corbett M 2009 *31st Int. Electric Propulsion Conf.*
- [39] Sercel C L, Gill T M and Jorns B A 2023 *AIAA Science and Technology Forum* (<https://doi.org/10.2514/6.2023-0449>)